Energy absorption of expansion tubes using a conical-cylindrical die: Theoretical model

Min Luo [a], Jialing Yang [b,*], Hua Liu [b], Guoxing Lu [c], Jilin Yu [d]

[a] Beijing Institute of Spacecraft System Engineering, Beijing 100094, PR China
[b] Institute of Solid Mechanics, Beihang University, Beijing 100191, PR China
[c] Faculty of Science, Engineering and Technology, Swinburne University of Technology, Hawthorn, VIC 3122, Australia
[d] CAS Key Laboratory of Mechanical Behaviour and Design of Materials, University of Science and Technology of China, Heifei, Anhui 230027, PR China

ARTICLE INFO

ABSTRACT

Previous experimental and numerical investigations have shown that expansion tubes under axial compression by a conical-cylindrical die had stable and efficient energy absorption characteristics [1]. In order to further understand the energy absorption mechanisms of such a tube expansion process, a theoretical analysis is given in this paper. The tube material is assumed to be rigid, linear hardening and the die is rigid. When the die is gradually pushed in, the tube expands. Both the radial deflection of the tube wall and the required driving force vary with the stroke of the die and their expressions are obtained theoretically. The final radius of the tube and the driving force in the steady-state are estimated. The theoretical analysis explains three deformation modes observed in the experiments [1]: tube tip-conical surface contact mode (T-C mode), tube wall-conical surface contact mode (W-C mode), tube wall-conical and cylindrical surface contact mode (W-CC mode), depending on the values of geometrical parameters of the tube and the die, such as the ratio of tube thickness to radius h/R_0 and the semi-angle of the die γ. Deformation characteristics in each mode are discussed and a map of phases in the $h - \gamma$ plane is given theoretically. The theoretical results are compared with the experimental data, with a reasonably good agreement. In addition, an analysis of the early deformation stage using elastic, linear hardening tube material model demonstrates that the elastic deformation of the tube is negligible.

1. Introduction

Circular tubes under axial compression are widely used as energy absorbers which have drawn much attention by researchers [2–4]. The deformation mechanisms of circular tubes under axial compression could be progress buckling, inversion, splitting or even expansion. The buckling behaviour of tubes has been studied for many years. Alexander [5] was the pioneer to provide a theoretical model for the axisymmetric fold of a circular tube. Abramowicz and Jones [6] proposed an effective crush length, and Wiezbicki et al. [7] introduced a parameter known as the eccentricity factor. Theoretical studies for the nonsymmetric buckling, also known as the diamond mode or Yoshimura mode, are less successful than those for the axisymmetric fold mode. Pugsley and Macaulay [8] were among the first researchers to consider the diamond mode. Johnson et al. [9] attempted to develop a theory for the diamond mode of PVC tubes based on experiments. Further theoretical studies were conducted by Singace [10]. More recently, Guillow et al. [11] provided a detailed experimental analysis and discussed the mode classification for circular 6060-T5 aluminum tubes. Using finite

element (FE) simulations, Karagiozova and Jones [12] examined the crushing behaviour of aluminum and steel cylindrical shells subjected to an axial impact. Bardi et al. [13] conducted a series of crushing experiments on moderately thick circular tubes and proposed a method to predict the onset of collapse. In addition to the circular tube, tubes with other section shapes (conical, square, rectangular, hexagonal, triangular and pyramidal) have been studied [14–16]. Another energy-absorbing mechanism by circular tubes is inversion. In 1966, Guist and Marble [17] made the first theoretical analysis to predict the steady knuckle radius and inversion force for the tube under free inversion. The most recent study on the free inversion of circular tubes was presented by Liu et al. [18]. Axial splitting of circular tubes by a cutter is also an effective energy absorption method. The splitting of thin-walled structure was first introduced by Stronge et al. [19]. Then, Reddy and Reid [20] investigated the splitting behaviour of circular metal tubes under both quasi-static and dynamic condition. Later, using a conical die instead of a curved one, Huang et al. [21] carried out similar work experimentally and theoretically. Li et al. [22] presented experimental and numerical investigations of expanding–splitting circular tubes recently.

Nomenclature

$d\theta$	small angle subtended by the arc of a strip from the tube wall cut along its axial direction (Fig. 5)
D, D_p	bending stiffness of tube wall in the elastic and strain hardening stages, respectively
E, E_P	elastic modulus and strain hardening modulus, respectively
f_0	frictional force per unit length
F_s	steady-state driving force
h	wall thickness of the tube
H	stroke of the die
L	tube length
M_x	bending moment per unit length in the meridional direction
M_s	fully plastic bending moment per unit length
N_x	axial membrane force per unit length
N_θ	membrane force per unit length in the circumferential direction
N_s	fully plastic membrane force per unit length
$P_{x0}, P_{y0},$	components of contact force in the axial and radial directions, respectively
Q_x	shear force per unit length
q	notation for N_θ / R_0
R_0	initial radius of the tube
R_D	radius of the cylindrical section of the die
T-C mode	tube tip - conical surface contact mode (Fig. 7)
W-C mode	tube wall - conical surface contact mode (Fig. 8)
W-CC mode	tube wall - conical and cylindrical surface contact mode (Fig. 9)
W	outward radial displacement of the tube wall
W_s	outward radial displacement of the tube wall in steady-state deformation
γ	semi-cone angle of the die
δ_0	critical length of deformation segment of the tube at the beginning of flaring
κ	axial curvature of the tube wall
υ	Poisson's ratio
σ_s	initial yield stress
μ	coefficient of friction
ϕ	inclined angle of tube wall segment

In addition to the energy dissipation mechanisms of circular tubes mentioned above, expansion of tubes is a very efficient and stable process for energy absorption. As shown in Fig. 1(a), a metal tube guided by a conical-cylindrical die and subjected to axial compression undergoes flaring and radial plastic expanding deformation. A typical load-displacement curve for quasi-static loading is shown in Fig. 1(b). The tube-expansion dissipates a large amount of energy through the plastic deformation of the tube and frictional work, eventually with a constant driving force during a long stroke. Experiments showed that the maximum value of specific energy absorption for aluminum tube-expansion can reach 25 kJ/kg [1]. Due to its stable driving force and high energy absorption efficiency, the expansion of tubes has drawn more and more attention in the field of energy-absorbing design in recent years. Lu [23] provided theoretical expressions which relate the flaring ratio, the tube end downward depth ratio, and the tube end strain rate to the tool stroke and the velocity in the tube flaring process. Fischer et al. [24] studied the tube flaring forming. They derived an analytical expression for the stress and strain fields as well as the driving force. Although initially the variation of wall thickness within the deformed region of the shell was approximated by a linear function, it was then concluded that the wall thickness may be regarded as a constant during the expansion process.

Daxner et al. [25] and Almeida et al. [26] investigated the buckling and fracture of the expansion tube by using a die. Shakeri et al. [27] proposed an analytical model to predict the mean crush load of the shock absorber with idealized rigid perfectly plastic material and frictionless interaction property. Seibi et al. [28] presented a comparative experimental and numerical study for both aluminum and steel tubes expanded at various expansion ratios and mandrel angles. Al-Abri and Pervez [29] established an analytical model describing the expansion process of a thick-wall solid tubular and discussed the influences of geometrical parameters and friction on the expansion force. Then, Yan et al. [30] proposed a theoretical model that considered the additional shear deformation and expansion ratio enlargement to predict the contact force. In Shakeri, Al-Abri, and Yan's theoretical models, the transition section of the tube was assumed to consist of three straight lines, corresponding to the undeformed section, the expanded section and the expanding section contacting with the conical die. Base on this assumption, the steady compressional force can be obtained by the energy conservation equations. To improve the above models, Liu and Qiu [31] proposed a more accurate theoretical model, in which the deformation mechanism was assumed to consist of three straight lines and two continuous curves between them. Moreover, two combined deformation processes of the expanding-splitting tube and expanding-folding tube were reported by Li et al. [32] and Chahardoli and Nia [33]. More recently, Liu et al. [34] improved their theoretical model by considering the effect of the die radius r_{die}. By introducing a critical die radius r^*_{die} and comparing it with the actual die radius r_{die}, they expanded different deformation modes observed in [1].

The theoretical works mentioned above were, however, based on the energy method, which were focused on the accuracy of the predicated steady compressive force and the final expanded radius. The mechanics for the early expanding stage when the tube was expanding along the conical section of the die could not be described. To obtain a further understanding of the whole expanding process, this paper presents a theoretical analysis based on the theory of axisymmetric deformation of cylindrical shell with a rigid, linear hardening material model. The expressions of the radial deflection of the tube wall and the required driving force vary with the stroke of the die are obtained theoretically. The theoretical analysis explains the three experimentally observed deformation i.e. T-C mode, W-C mode and W-CC mode [1]. In the first two modes, the magnitude of the steady driving forces F_s are calculated approximately from the energy balance method. In addition, an elastic, linear hardening material model is adopted for the early stage of deformation process to investigate any possible consequence of neglecting the elastic deformation. Finally, based on the theoretical analysis, the *F-H* curves (i.e., driving force vs. stroke of the die) of the three deformation modes, a map of deformation modes in the $h-\gamma$ plane, and effects of strain hardening modulus and frictional coefficient are given and compared with the experimental results, respectively.

2. Basic assumptions in analytical model

The theoretical analysis in the following sections for the axisymmetric tube expansion is under four assumptions as explained in detail below.

Firstly, the tube material is assumed rigid, linear hardening and the die is rigid. In the experimental study [1], 5A06 aluminum tubes and high strength structure steel dies were used. As the tubes are much deformable compared with the steel die, the plastic deformation is mainly in the tubes and the die may be reasonably regarded as rigid. The stress-strain curve from a standard tensile test of the tube material is shown in Fig. 2, in which it can be seen that the elastic deformation is very small and negligible. Furthermore, the stress-strain curve may be approximated by a rigid, linear hardening (dotted line) material model (See Section 5.1). This idealisation is conventionally employed for analyzing energy absorbing devices as they usually experience large plastic
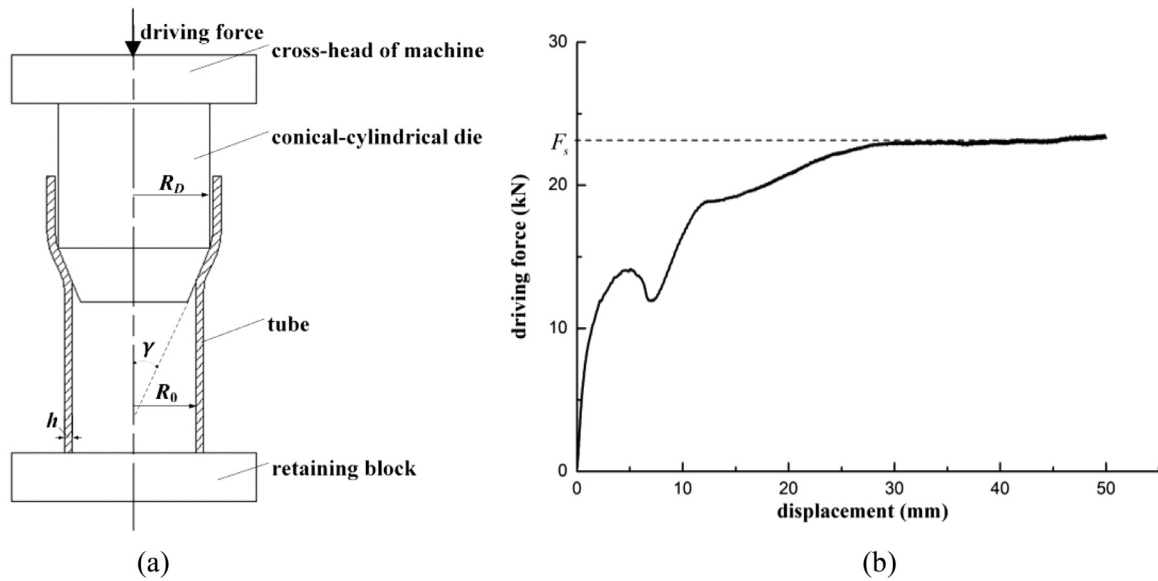
Fig. 1. Expansion of tube using conical-cylindrical die: (a) Schematic representation; (b) Typical load-displacement curve.
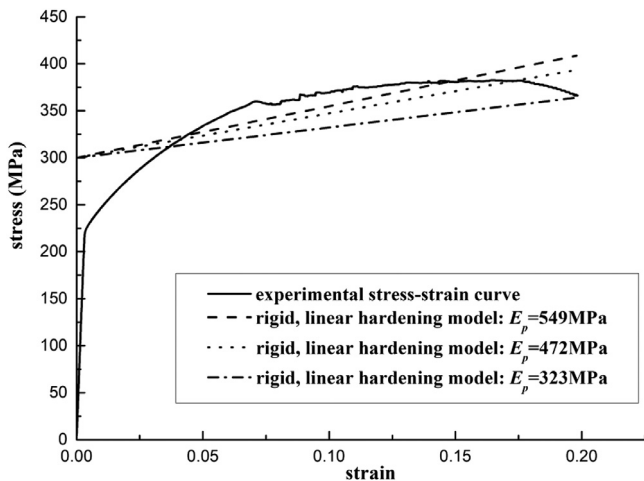

Fig. 2. Experimental and idealized stress-strain curve for 5A06-T5 rustproof aluminum.

Fig. 3. Force-displacement curves obtained by experiments and FE simulations for tube-expanding process in Ref. [1]. Excellent agreement between experiment and FEM curves could be found when $\mu= 0.05$.

deformation. The stress-strain relationship is, hence, given by,

$$\sigma = \sigma_s + E_p \varepsilon \tag{1}$$

where σ_s is the yield stress and E_p is the strain-hardening modulus. For 5A06 aluminum alloy shown in Fig. 2, it is found that σ_s=300 MPa and E_p=549 MPa. These values were obtained by drawing a straight line from the point corresponding to the necking strain (15%) such that the area under the idealized stress-strain curve is the same as the experimental stress-strain curve. There are, of course, other ways of approximating the stress-strain curve, such as by drawing a tangent line from the initial yield stress, which would lead to other values. Theoretical predictions are discussed in Section 5.4 for other values of E_p, which may be lower than 549 MPa.

Secondly, a classical Coulomb friction model with a constant frictional coefficient (μ=const) is used. To facilitate the smooth tube expansion by a die in the experiment, Lithium-based grease containing MoS$_2$ solid lubricant was used to reduce the friction between the tube wall and the die surface. In practice, the contact surface between the tube and the die was fully lubricated and the value of the frictional coefficient should be very small (less than 0.15), but it was difficult to determine
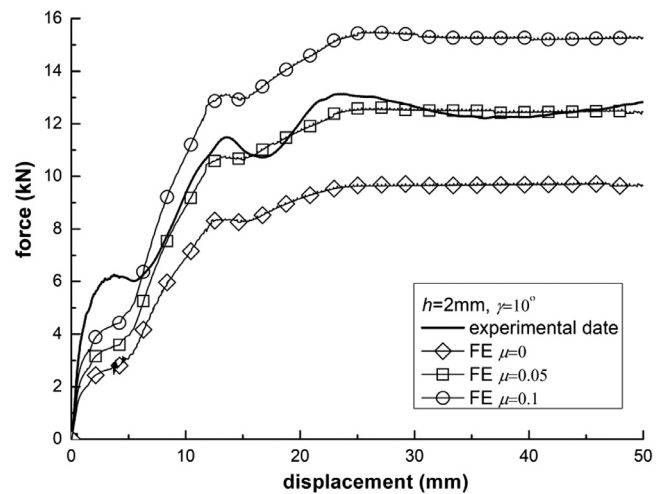
accurately. As shown in Fig. 3, it was found [1] that the FE simulation fits the experimental data very well when $\mu = 0.05$, while a frictionless contact $\mu = 0$ underestimates the driving force by approximately 22% and a coefficient of friction of $\mu = 0.2$ overestimates the force by 18%. Therefore, $\mu = 0.05$ is used in the theoretical analysis. Furthermore, the influence of a small variation in the value of the frictional coefficient on the theoretical forces is discussed in Section 5.4.

Thirdly, the tube thickness is assumed to remain constant during tube expansion. Fischer et al. [24] has shown theoretically that the strain in the direction of thickness is negligible in the tube flaring process and suggested the tube thickness may be assumed constant. This has also been verified in our experiment [1]. Intuitively, this is because the tensile circumferential strain is compensated by the compressive axial strain, with the total volume of the material keeping constant.

Finally, for a cylindrical shell under axisymmetric loading, there is no coupling between the axial bending moment and the circumferential membrane force in the yield criterion. Consequently, an element on the tube wall will yield only if the circumferential membrane force reaches the fully plastic membrane force ($N = N_s$), or the axial bending moment
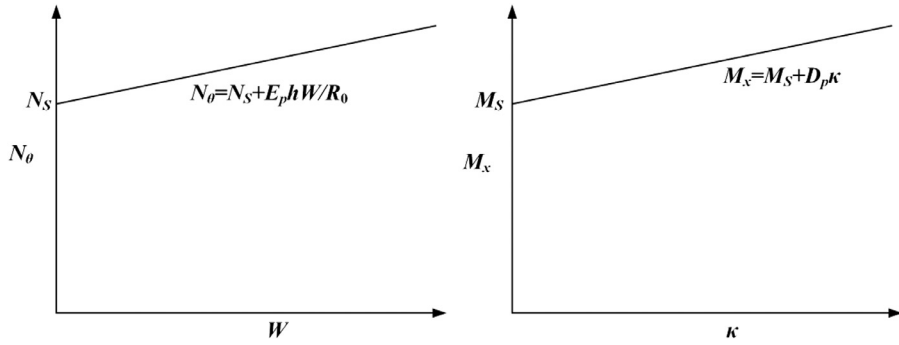
reaches the fully plastic moment ($M = M_s$). Hodge [35] has discussed different yield conditions for cylindrical shells under axisymmetric loading and successfully carried out theoretical plastic limit analysis with the uncoupled yield condition.

For a circular tube with rigid, linear strain-hardening material from Eq. (1) and an outward radial displacement W, the circumferential membrane force and the axial bending moment per unit length, respectively, are given by

$$N_\theta = N_s + \frac{E_p h}{R_0} W \ \left(\text{if} \ N_\theta \geq N_s \right) \tag{2}$$

$$M_x = M_s + D_p \kappa \ \left(\text{if} \ M_x \geq M_s \right) \tag{3}$$

where $N_s = \sigma_s h$, $M_s = \frac{\sigma_s h^2}{4}$, $\kappa = \frac{d^2 W}{dX^2}$, and $D_p = \frac{E_p h^3}{12(1-\nu^2)}$ are, respectively, the fully plastic membrane force, the fully plastic axial bending moment, the axial curvature, and the bending hardening rigidity. The circumferential membrane force-radial displacement and the axial bending moment-curvature relationships are sketched in Fig. 4.

3. Analysis for three deformation modes

An axisymmetrically deformed cylindrical shell and the free body diagram for the small element cut from it are shown in Fig. 5. The axial length of the element is dX. The arc subtending angle is $d\theta$ and its length is $R_0 d\theta$. The internal forces acting on the element are the axial force $N_x R_0 d\theta$, the circumferential force $N_\theta dX$, the shear force $Q_x R_0 d\theta$, and the axial bending moment $M_x R_0 d\theta$. The external distributed loads per unit area are q_x and q_n in the axial and normal directions, respectively. From the equilibrium conditions of the element, we have the following equations:

$$\frac{dN_x}{dX} + q_x = 0 \tag{4}$$

$$\frac{dQ_x}{dX} + \frac{N_\theta}{R_0} + q_n = 0 \tag{5}$$

$$\frac{dM_x}{dX} - Q_x = 0 \tag{6}$$

When the tube expands by the die, the external distributed loads $q_x = q_n = 0$ except on the contact area between the die and the tube wall. Thus, from Eqs. (5) and (6), an equilibrium equation can be obtained, as follows,

$$\frac{d^2 M_x}{dX^2} + \frac{N_\theta}{R_0} = 0 \tag{7}$$

With the constitutive relations and appropriate boundary conditions of the tube, equilibrium Eq. (7) can be solved. Solutions will be given in the following sections.

Fig. 6 shows a strip OB which is isolated along the axial direction of the tube and has the arc cross-section subtending a small angle $d\theta$. The tube wall does not deform until the driving force F reaches a critical
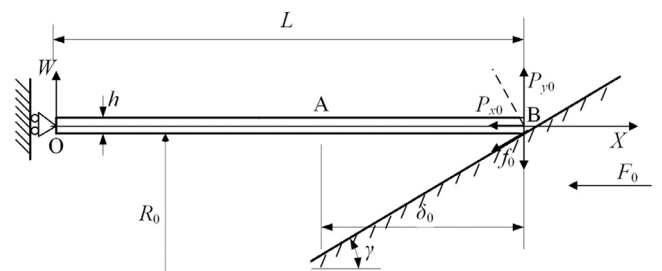

Fig. 6. Sketch of the initial stage of the deformation process for the axial strip element isolated from the tube with the arc subtending a small angle $d\theta$.

value F_0, and the plastic bending deformation occurs at Point A, at a distance δ_0 from the tip (or $X = L - \delta_0$ away from the origin O), in Fig. 6. This takes place when the bending moment M_x reaches the fully plastic bending moment M_s, according to the uncoupled yield condition (the last assumption in Section 2). Three forces acting at the expanding end of the tube (Point B) are shown: the axial and radial components of the contact force per unit length of the contact circumference, P_{x0}, and P_{y0}, and the frictional force f_0. The circumferential membrane force is not shown. In the radial direction, this strip is in equilibrium under three forces: P_{y0}, the radial component of the circumferential membrane force and that of the frictional force f_0. For simplicity, $q = N_\theta / R_0$ is used below and then the radial component of the circumferential membrane force per unit length acting on the straight sides of the strip is $N_\theta d\theta = qR_0 d\theta$. When F reaches the critical value F_0 which corresponds to the onset of the plastic deformation on the tube wall, $M_x = M_s$ at A and $N_\theta = N_s$. From geometry relation, it follows,

$$P_{x0} = P_{y0} \tan \gamma, \quad f_{x0} = \mu P_{y0} \tag{8}$$

in which f_{x0} is the axial component of frictional force per unit length on the contact circle. Then P_{y0} and δ_0 can be easily derived from the equilibrium of the strip segment AB in the radial direction and the moment balance about A as

$$\delta_0 = \sqrt{\frac{R_0 h}{2}}, \quad P_{y0} = \frac{1}{(1 - \mu \tan \gamma)} \frac{\sigma_s h}{R_0} \sqrt{\frac{R_0 h}{2}} \tag{9}$$

The corresponding initial driving force F_0 is given as

$$F_0 = \frac{2\pi \sigma_s h (\tan \gamma + \mu)}{1 - \mu \tan \gamma} \sqrt{\frac{R_0 h}{2}} \tag{10}$$

When the driving force is larger than the initial critical force F_0, the tube will be flared along the conical surface of the die. Based on the contact behaviour between the tube and the die surface, at the conical part and cylindrical part of the die, respectively, the deformation process can be classified into three modes, i.e., T-C mode, W-C mode and W-CC mode. The deformation processes of these three modes are shown in Figs. 7, 8, and 9, respectively. In the previous experimental

Fig. 7. Three deformation stages of the tube in T-C mode, comparing with numerical case h=3 mm and γ=20° in Ref. [1]. (a) Stage A: tube is flared along the conical part of the die ($H < H_C$). (b) Stage B: tube continues its expanding along the cylindrical part of the die ($H_C \leq H < H_D$). (c) Stage C: the inward bending moment of the tube on the cylindrical part of the die reaches the linear hardening plastic range ($H_D \leq H < H_m$).

Fig. 8. Stage B, C and D in W-C mode, comparing with numerical case $h=2$ mm and $\gamma=10°$ in Ref. [1]. (a) Stage B: the tube is flared along the conical surface of the die with the inner face fully contacting the die ($H_E < H < H_C$). (b) Stage C: tube continues its expanding along the cylindrical part of the die ($H_C \leq H < H_D$). (c) Stage D: inward bending moment of the tube on the cylindrical part of the die reaches the linear hardening plastic range ($H_D \leq H < H_m$).

and numerical investigations in [1], the three deformation modes have been observed for a series of specimens with different tube thicknesses $h=1, 2, 3, 5$ mm ($R_0 = 22.5$ mm) and semi-cone angles of dies $\gamma = 5°, 10°$, $15°, 20°$. The numerical deformation results of three cases $h = 3$ mm and $\gamma = 20°$, $h = 2$ mm and $\gamma = 10°$, and $h = 1$ mm and $\gamma = 5°$, which represent typical examples of T-C, W-C, and W-CC modes, are added into Figs. 7 – 9 to show clearly the consistency between the proposed deformation model and numerical analysis.

In the T-C mode, the tip of tube (B) first contacts the conical surface in a point-contact manner. When the die moves in further, only the same point of the tube (B) remains in contact with the conical surface (Fig 7(a)). After point B moves over the shoulder of the die (Q), the upper portion of the tube expands continuously, and loses contact with the die, i.e., only the shoulder Q touches the tube (Fig. 7(b)). When the tube moves further, the upper portion of the tube begins to bend inwardly initiated at Q (Fig. 7(c)).

In the W-C mode, after the initial point contacts between the tube tip B and the conical surface, as the die moves in further, the tube wall comes in touch with the conical surface and the contact area there-

fore increases (Fig. 8(a)). However, after the tube material has moved over the shoulder of the die, the contact area with the conical surface decreases and the upper portion of the tube expands continuously (Fig. 8(b)). When the tube moves further, the upper portion of the tube begins to bend inwardly initiated at Q (Fig. 8(c)), the same as the case for the T-C mode.

In the W-CC mode, the initial stage when the tube is in touch with the conical surface is the same as in the W-C mode (Fig. 9(a)), i.e., the contact is the surface contact instead of a point contact (as in the T-C mode). After the material has moved over the die shoulder, however, this portion of the tube wall remains in full contact with the cylindrical surface of the die (Fig. 9(b)). Analyses of these three modes are given, respectively, as follows.

3.1. T-C mode

The deformation process in the T-C mode is characterized by the fact that only the tube tip B contacts the conical surface of the die until it reaches the intersection of the conical section and the cylinder section
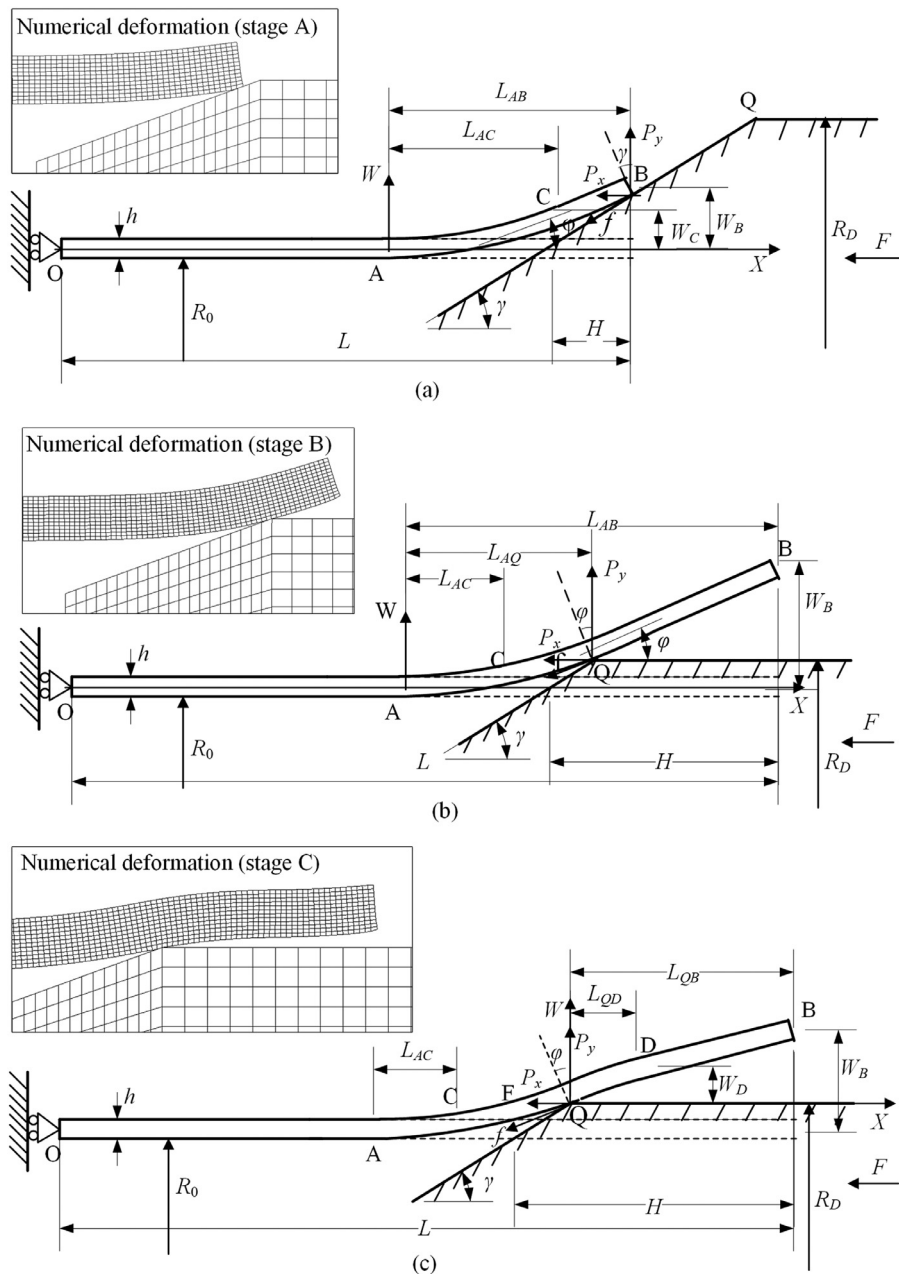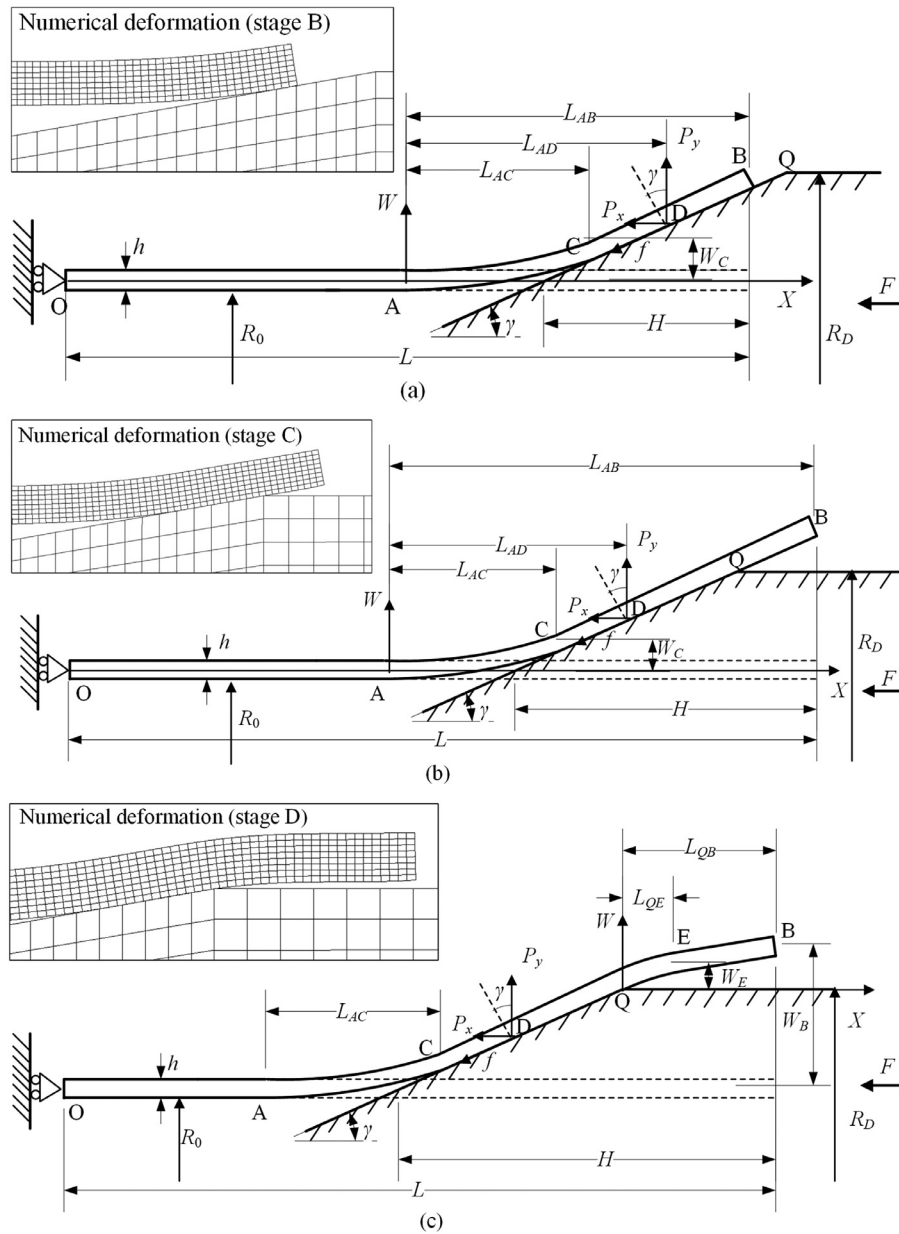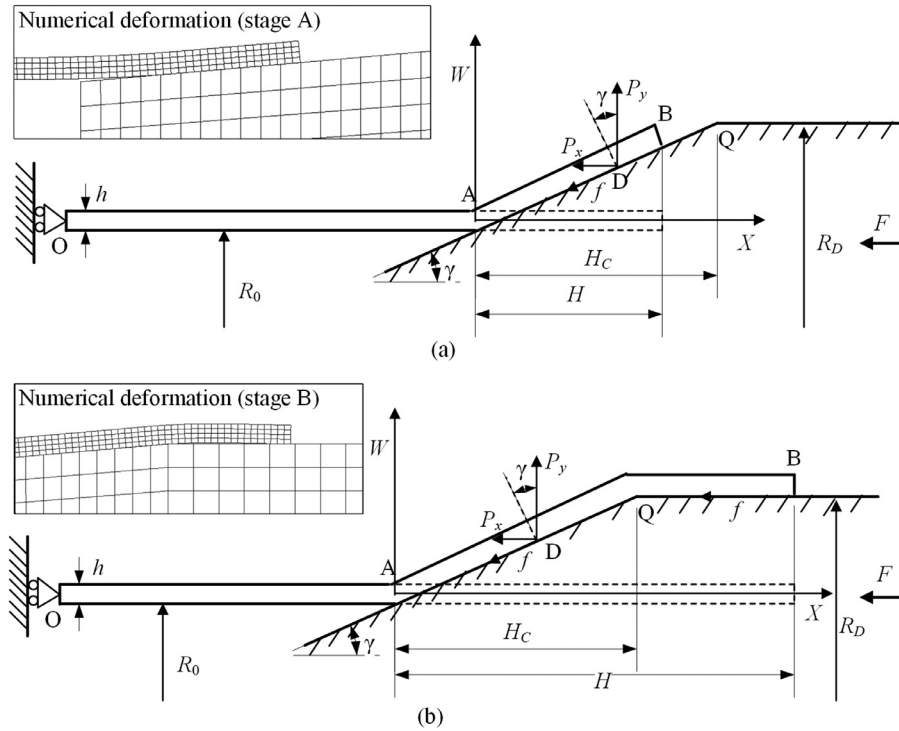
Fig. 9. Analysis of the deformation of the tube in W-CC mode, comparing with numerical case $h=1$ mm and $\gamma=5°$ in Ref. [1]. (a) Stage A: the tube is flared along the conical part of the die ($H < H_C$). (b) Stage B: tube continues its expanding along the cylindrical part of the die ($H_C \leq H$).

of the die, or the shoulder Q in Fig. 7. It means that the slope of the tube wall at B is always smaller than the semi-angle of the die γ. The complete deformation process of this mode can be described as three stages before the driving force reaches a steady state, as illustrated in Fig. 7: stage A, the tube expands along the conical surface of the die; stage B, the tube tip is pushed over the shoulder Q and the tube continues its expanding process along the cylindrical part of the die; stage C, the inward (reverse) bending moment of the tube above the cylindrical section of the die reaches M_s at Q, and reverse bending deformation occurs near the region soon afterwards.

3.1.1. Stage A, tube expanding along the conical section of the die

When the driving force is above the initial force F_0, the end of the tube will be expanded along the conical surface of the die. A strip OB isolated from the tube in the axial direction with the arc subtending a small angle $d\theta$ is considered for its equilibrium, as seen in Fig. 7(a). The tube strip may be divided into three segments: segment AC bends outward with bending moment larger than M_s (due to strain hardening), and segments OA and CB remain straight with the bending moment smaller than M_s, as shown in Fig. 7(a). For specimens with large bending rigidity and large semi-angle of the die, angle ϕ (which is defined as the angle between segment CB and the axial direction) is always smaller than γ during the flaring of the expanding end of tube, B, from the initial position to the shoulder of the die (point Q).

Setting up a coordinate system W-X at Point A and substituting Eqs. (2) and (3) into (7), the equilibrium equation of axisymmetrically loaded tube can be expressed in terms of W, as follows:

$$D_P \frac{d^4W}{dX^4} + \frac{E_p h}{R_0^2} W + \frac{N_s}{R_0} = 0 \tag{11}$$

The solution of the above differential equation is,

$$W = e^{kX}\left(C_1 \cos kX + C_2 \sin kX\right) + e^{-kX}\left(C_3 \cos kX + C_4 \sin kX\right) - \frac{N_s R_0}{E_p h} \tag{12}$$

where $4k^4 = \frac{E_p h}{R_0^2 D_P}$.

To satisfy the continuity condition at C of segment AC, the displacement function of the rigid segment CB can be assumed as $W_{CB} = \tan\phi(X - L_{AC}) + W_C$, where ϕ is the inclined angle of CB. With the notation q introduced before and Eq. (2), it follows,

$$q = \frac{N_s}{R_0} + \frac{E_p h}{R_0^2}\left(\tan\varphi\left(X - L_{AC}\right) + W_C\right) \tag{13}$$

Thus, the equilibrium equations of strip segment CB are,

$$P_y(1 - \mu\tan\gamma + \tan\varphi\tan\gamma + \mu\tan\varphi)\left(L_{AB} - L_{AC}\right)$$
$$- \int_{L_{AC}}^{L_{AB}} q\left(X - L_{AC}\right)dX = M_s \tag{14}$$

and

$$P_y(1 - \mu\tan\gamma) = P_{yC} + \int_{L_{AC}}^{L_{AB}} q\,dX \tag{15}$$

where P_{yC} is the radial force of segment AC at point C. With the boundary conditions at A: $W = W' = 0$ and $M_x = M_s$, and the continuity conditions at C: $M_x = M_s$ and $P_{yC} = -D_p W'''$ with $W' = \tan\phi$, the unknown coefficients $C_1 \sim C_4$, L_{AC}, L_{AB}, P_y, P_{yC} and the deflection of segments AC and CB in terms of W_B can be solved from Eqs. (12), (14) and (15). Thus, the driving force can be expressed as

$$F = 2\pi R_0 P_y(\tan\gamma + \mu) \tag{16}$$

and the stroke of the die is

$$H = \frac{W_B}{\tan\gamma} \tag{17}$$

For the T-C mode the inclined angle ϕ increases with the stroke.

3.1.2. Stage B, tube expanding along the cylindrical part of the die

When the tip of the tube, B, reaches the shoulder of the die (Q in Fig. 7), the corresponding stroke of the die, denoted as H_C, is given by

$$H_C = \frac{R_D - R_0}{\tan\gamma} \tag{18}$$

As the die is pushed, the tube tip, B, will cross over the shoulder Q when $H > H_C$, and the front part of the tube continually undergoes

expansion as seen in Fig. 7(b). The current deformed tube wall is composed of the bent segment, AC, with bending moment larger than M_s, and the straight segment CB with bending moment smaller than M_s. In this case, the equilibrium equation of segment AC is the same as Eq. (11). It should be noted that the contact force and the frictional force between the tube and the die always act at point Q, but the direction of the contact force changes to be perpendicular to the axis of the tube. Thus, the equilibrium equations for segment CB are,

$$P_y\left(1 + \tan^2\varphi\right)\left(L_{AQ} - L_{AC}\right) - \int_{L_{AC}}^{L_{AB}} q\left(X - L_{AC}\right)dX = M_s \qquad (19)$$

$$P_y(1 - \mu\tan\varphi) = P_{yC} + \int_{L_{AC}}^{L_{AB}} q\,dX \qquad (20)$$

where $L_{AQ} = \frac{R_D - R_0 - W_C}{\tan\varphi} + L_{AC}$. With boundary conditions at A and continuity conditions at C, the deflection functions of segments AC and CB and the contact force P_y can be solved for a given value of W_B. Hence the driving force and the stroke of the die are,

$$F = 2\pi R_0 P_y(\tan\varphi + \mu) \qquad (21)$$

$$H = H_C + \frac{W_B - R_D + R_0}{\tan\varphi} \qquad (22)$$

As indicated above, when tip B crosses over Q, the direction of the contact force changes from being normal to the conical surface to that of the cylindrical surface. Therefore, the driving force drops abruptly due to this change in the direction of the contact force. This phenomenon, which was also observed in the experiments [1], is an important characteristic of the T-C mode and will be discussed with examples in Section 5.2.

3.1.3. Stage C, inward bending of the tube wall over the cylindrical section of the die

In stage B, the bending moment and the curvature within segment CB can be easily calculated from the deflection. In stage C, we find that condition $|M_x| < M_s$ is satisfied over segment CB and the maximum inward bending moment occurs at Q. When the bending moment at Q reaches $M_{xQ} = -M_s$ (outward direction is defined as positive), the corresponding stroke of the die is denoted as H_D. The bending moment in the vicinity of Q is in the linear hardening range when $H > H_D$. The bending moment in segments AC, FQ, and QD is in the linear hardening range and that in segments CF and DB is smaller than M_s. Thus, segments AC, FQ, and QD bend, while segments CF and DB are straight, as shown in Fig. 7(c). Because the length of all these segments is unknown, i.e. the boundaries between the deforming and rigid segments are undetermined, equations for all these segments need to be solved simultaneously, which might not be straightforward. The solution procedure can be greatly simplified if the inclined angle of QD at Q is assumed to be fixed and approximately equals to ϕ. Therefore, setting up a coordinate system W-X at point Q, the equilibrium equation of segment QD is,

$$D_P \frac{d^4W}{dX^4} + \frac{E_p h}{R_0^2} W + \frac{N_s}{R_0} + \frac{E_p h}{R_0^2}\left(R_D - R_0\right) = 0 \qquad (23)$$

The deflection of rigid segment DB is given as $W_{DB} = W'_D(X - L_{QD}) + W_D$, where W'_D and W_D are to be determined. Similarly, with the notation q defined above and Eq. (2), it follows,

$$q = \frac{N_s}{R_0} + \frac{E_p h}{R_0^2}\left(W_D'\left(X - L_{QD}\right) + W_D + R_D - R_0\right) \qquad (24)$$

The equilibrium equations of segment DB are,

$$P_{yD} + \int_{L_{QD}}^{L_{QB}} q\,dX = 0 \qquad (25)$$

$$\int_{L_{QD}}^{L_{QB}} q\left(X - L_{QD}\right)dX = M_S \qquad (26)$$

Applying the boundary conditions at Q: $W = 0$ and $W' = \tan\phi$, and the continuity conditions at D: $M_x = -M_s$, $P_{yD} = -D_p W'''$, $W' = W'_D$ and

$W = W_D$, the deflection of segments QD and DB can be obtained from (23)–(26) for a given L_{QB}.

The results show that the deflection at B, W_B, increases with L_{QD} and reaches its maximum value W_{max} when the stroke is H_m, which is very close to H_D. Hence stage C is very short, unloading and reverse yielding in the circumferential membrane N_θ subsequently occurs from the tube tip B if W_B decreases. The experimental and numerical analyses show that a steady-state driving force is attained after this complex unloading and reverse yielding process [1]. During the steady-state, the magnitude of the driving force, F_s, can be calculated approximately by the energy method, which will be shown in Section 4.

3.2. W-C mode

As mentioned above, in the T-C mode, the angle ϕ is smaller than γ when the tube tip B reaches point Q. But for specimens with weak bending rigidity and dies with a smaller semi-angle, the angle ϕ may increase and be equal to γ before the tube tip B reaches point Q, which means that the inner wall of the tube may contact the conical surface of the die. The deformation process of the W-C mode can be described in four stages before the driving force finally reaches a steady state. In stage A, the tube is flared along the conical section of the die and only its tip contacts the cone-surface of the die. In stage B, when the tube is further flared along the conical part of the die, the inner surface of the tube contacts the die. In stage C, the tube tip B moves over the die shoulder Q and continues its expanding process along the cylindrical part of the die. Finally in stage D, inward plastic bending of the tube occurs.

The analysis of stage A is the same as that for the T-C mode, referring to Fig. 7(a). The deflection at the tube end B increases with the stroke of the die. When the angle ϕ increases to γ, stage A ends and the corresponding stroke is denoted as H_E. After that, the tube is flared with the inner surface contacting the cone-surface of the die, as illustrated in Fig. 8(a).

There is now a distributed force over the contact area – segment CB. As the segment remains straight, the resultant of the distributed force is equivalent to a concentrated force P acting at D, whose position is to be determined. The equilibrium equation of segment AC is the same as Eq. (11) and the equilibrium equations for segment CB are

$$P_y\left(1 + \tan^2\gamma\right)\left(L_{AD} - L_{AC}\right) - \int_{L_{AC}}^{L_{AB}} q\left(X - L_{AC}\right)dX = M_s \qquad (27)$$

$$P_y(1 - \mu\tan\gamma) = P_{yC} + \int_{L_{AC}}^{L_{AB}} q\,dX \qquad (28)$$

where L_{AD} is the X-coordinate of D, at which the equivalent concentrated contact force acts, and q can be obtained from Eq. (13) by letting $\phi = \gamma$. Eqs. (11), (27), and (28) can be solved with the boundary conditions at A and continuity conditions at C, and the F-H curve is obtained from Eqs. (16) and (17).

Stage B finishes when the tube tip reaches point Q, at $H = H_C$. It should be noted that the direction of the contact force does not change when $H = H_C$ as ϕ equals γ. Therefore, unlike the case of the T-C mode here there is no sudden change in the driving force. The tube continues its expansion before the bending moment at Q reaches $-M_s$, and then stage C begins. When stage C finishes, the bending moment in the vicinity of Q is in the linear hardening state, the inward bending occurs over the corresponding section and stage D begins. The deflection of B, W_B, increases and reaches its maximum value W_{max} in stage D. The analysis of stages C and D in W-C mode is similar to that of stages B and C in the T-C mode, respectively.

3.3. W-CC mode

Experimental data and numerical results [1] show that for tubes with much weak bending rigidity and dies with small semi-angle, the deformed tube wall conforms to the surface of the conical and cylindrical

sections of the die, except for a very short gap around Q. Therefore, the progressive push of the die makes the contact area between the tube wall and the die surface increase, as well as the frictional force. As a result, the driving force also increases all the time. Consequently, there is no steady-state force for this deformation mode. The bending deformation may be neglected and a simplified analysis can be obtained. The deformation of the tube in the W-CC mode can be described in two stages: in stage A, the tube is flared along the conical part of the die; in stage B, it is along the cylindrical part of the die.

When the stroke of the die is shorter than H_C, as shown in Fig. 9(a), the tube is flared along the conical part of the die. Neglecting the bending deformation around the rigid corner at A, the deflection of segment AB is,

$$W = X \tan \qquad (29)$$

With the notation $q = N_\theta / R_0$ defined above and substituting Eq. (29) into Eq. (2), it follows,

$$q = \frac{N_s}{R_0} + \frac{E_p h}{R_0^2} X \tan \gamma \qquad (30)$$

Thus, the equilibrium equation of segment AB is,

$$P_y (1 - \mu \tan \gamma) = \int_0^H q \, dX \qquad (31)$$

Substituting Eq. (30) into Eq. (31), the *F-H* relationship can be obtained from Eq. (16), i.e.

$$F = \frac{2\pi(\mu + \tan \gamma)H}{1 - \mu \tan \gamma} \left[N_s + \frac{E_p h \tan \gamma}{2R_0} H \right] \qquad (32)$$

When the stroke is longer than H_C, the tube is expanded along the cylindrical part of the die, as shown in Fig. 9(b), with a small gap caused by the bending deformation of the tube wall at Q. Neglecting the bending deformation around the rigid corner at Q, hence N_θ on contact area QB is a constant. Using Eq. (2), q is obtained as

$$q = \frac{N_s}{R_0} + \frac{E_p h}{R_0^2} (R_D - R_0) \qquad (33)$$

Thus the total frictional force on contact area QB is given by:

$$f = 2\pi \mu R_0 (H - H_C) q \qquad (34)$$

Hence, the driving force during stage B can be calculated as

$$F = \frac{2\pi H_C (\mu + \tan \gamma)}{1 - \mu \tan \gamma} \left[N_s + \frac{E_p h (R_D - R_0)}{2R_0} \right]$$
$$+ 2\pi \mu (H - H_C) \left[N_s + \frac{E_p h}{R_0} (R_D - R_0) \right] \qquad (35)$$

where H_C can be obtained from Eq. (18). It is clear that the driving force increases with the stroke and there is no steady-state force in the W-CC mode.

4. Steady-state driving force F_s

As mentioned above, in the T-C mode and the W-C mode a complex unloading and reverse yielding in the circumferential membrane may take place after the tube tip reaches its maximum value $W_{\max}$. Experiments and numerical simulations have demonstrated that the tube deformation tends to a stable state eventually and the driving force approaches a steady-state value F_s, which is a direct indication of the energy absorption capacity [1]. It is not straightforward to give a theoretical analysis for the unloading and reverse yielding and thus it is difficult to obtain an exact expression for the steady-state force. In this section an estimate of this steady-state force by using the energy balance method is given.

The work done by the external force during the die pushing process is dissipated by plastic bending, circumferential stretching of the tube, and the friction between the tube and the die. When the die is moving forward with a speed v_0, the rate of the external work is equal to the energy dissipation rate by the tube,

$$F_s v_0 = \dot{E}_s + \dot{E}_b + \dot{W}_f \qquad (36)$$

where $\dot{E}_s$, $\dot{E}_b$, and $\dot{W}_f$ denote the rate of energy dissipation in plastic stretching, bending, and friction, respectively.

The plastic energy dissipated depends on the plastic strain of the tube in the steady state. Neglecting the complex unloading and reverse yield process that occurs near the expanding end of the tube, the profile in the steady deformation state of the T-C mode is shown in Fig. 10. Segments AC and FD bend in the opposite directions with the bending moment in the linear hardening stage. Segments CF, DE, and EB are straight. The steady-state radial deflection in segment EB is W_s. Here, a method which is similar to that in Section 3.1.3 is employed to find W_s. The inclined angle of QD at Q is assumed approximately equal to ϕ. Then the equilibrium equations of segments QD and DE are the same as Eqs. (23), (25), and (26). Applying the boundary conditions at Q: $W = 0$, $W' = \tan \phi$ and at D: $W'_D = 0$, $M_x = -M_s$, $P_{yD} = -D_p W'''$, the deflections of QD and DE can be solved and W_s is calculated.

The energy dissipated in plastic stretching is mainly contributed from the circumferential stretching over the region between A and D, as seen in Fig. 10. The circumferential strain rate is

$$\dot{\epsilon}_\theta = \frac{v_0 \tan \gamma}{R_0} \qquad (37)$$

The volume of the element dX at coordinate X is,

$$dV = 2\pi h (R_0 + X \tan \varphi) dX \qquad (38)$$

Hence the rate of stretching energy is given by the integration of the product of the circumferential stress and strain rate over the volume of the deformation zone, which is

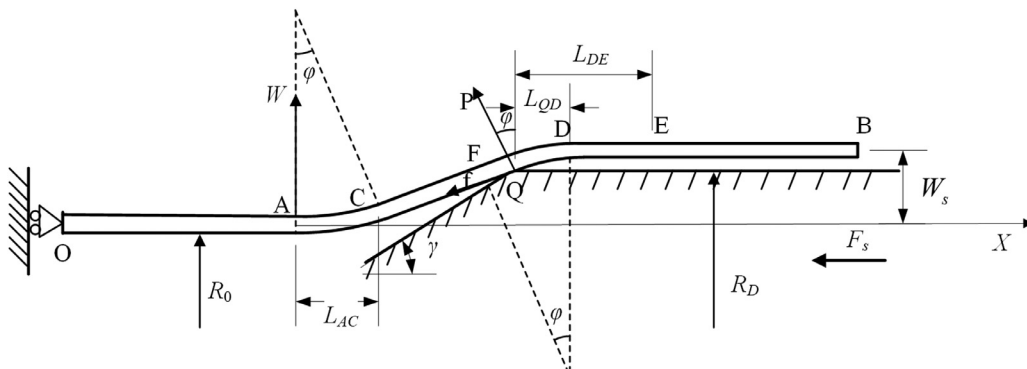$$\dot{E}_s = \int_v \frac{N_\theta}{h} \dot{\epsilon}_\theta \, dV \qquad (39)$$

Fig. 10. Sketch of the steady-state deformation of an expanding tube.

Thus, using Eq. (2) and assuming AD being a straight line of $W = X\tan\phi$, the rate of stretching energy is expressed as

$$\dot{E}_s = \frac{2\pi v_0 \tan\gamma}{R_0 \tan\varphi}\left[N_s R_0 W_s + \frac{1}{2}\left(N_s + E_p h\right)W_s^2 + \frac{E_p h W_s^3}{3R_0}\right] \tag{40}$$

As shown in Fig. 10, the rate of bending energy includes that in segments AC and FD. For the strip, segment AC bends in the anti-clockwise direction by an angle ϕ, and segment FD by the same angle ϕ but in an opposite direction. Therefore, the bending energy for segment FQ is approximately the same as that for segment AC. The average curvature of segment AC is,

$$\kappa_{AC} = \frac{\sin\varphi}{L_{AC}} \tag{41}$$

Thus, the energy dissipation rate by plastic bending is

$$\dot{E}_b = 4\pi R_0 M_s v_0 \left(\frac{\sin\varphi}{L_{AC}}\right) \tag{42}$$

The rate of energy dissipation by frictional force is

$$\dot{W}_f = 2\pi R_0 \mu P v_0 \tag{43}$$

where P is the normal contact force per unit length, and it is related to the driving force F_s as follows:

$$P = \frac{F_s}{2\pi R_0(\sin\varphi + \mu\cos\varphi)} \tag{44}$$

Substituting Eqs. (40), (42), and (43) into Eq. (36), the driving force in the steady-state is

$$F_s = \frac{2\pi(\sin\varphi + \mu\cos\varphi)}{\sin\varphi - \mu(1 - \cos\varphi)}$$
$$\times\left\{\frac{\tan\gamma}{\tan\varphi}\left[N_s W_s + \frac{W_s^2}{2R_0}\left(N_s + E_p h\right) + \frac{E_p h W_s^3}{3R_0^2}\right] + \frac{2R_0 M_s \sin\varphi}{L_{AC}}\right\} \tag{45}$$

Here the steady-state driving force of the T-C mode is obtained. As mentioned in Section 3.2, the driving force approaches a steady-state value in the W-C mode after stage D. From Sections 3.1 and 3.2, it can be concluded that the deformation process of stage D in the W-C mode is similar to that of stage C in the T-C mode. Thus, the analysis of steady-state F_s in the W-C mode is also similar to that in the T-C mode, which is not described in this paper.

A program has been written to calculate W_s, ϕ, L_{AC}, and then the value of the steady-state force can be estimated. The values of the steady-state driving force for different conditions are compared with the experimental data from [1], as shown in Fig. 11. In the experiments, aluminum
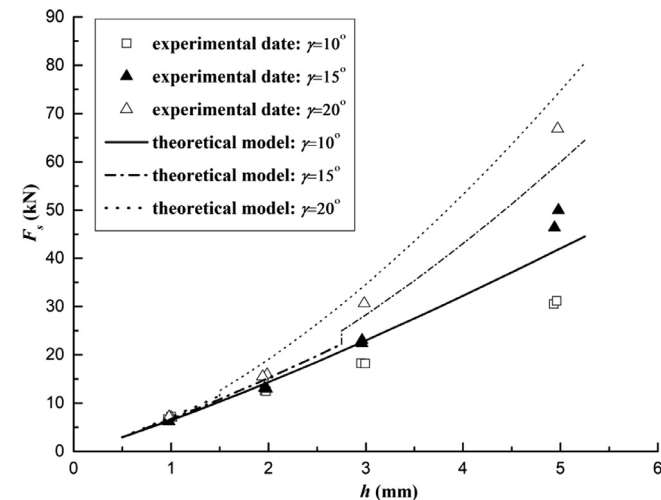

Fig. 11. Comparison of steady-state driving force measured from Ref. [1] and predicted by theory.

alloy 5A06 tubes with an inner radius of 22.5 mm and thickness of 1.0, 2.0, 3.0, and 5.0 mm were used and the dies were made of 30CrMoSiA structural steel with a semi-angle of 10°, 15° and 20°, respectively. The stress-strain curve of aluminum alloy 5A06 in tension can be idealized as rigid, linear hardening with an initial yield stress of 300 MPa and a hardening modulus of 549 MPa. The frictional coefficient $\mu = 0.05$ was determined by matching the experimental data with the analytical results. The comparison in Fig. 11 indicates that the theoretical values for F_s are in reasonable agreement with the experiments and the average error compared with experimental results is about 12%. Besides, the relative error increases with increasing γ and h. It is evident that for larger values of γ, larger values of F_s are needed and this is more pronounced for thick tubes. Although the theoretical values are, in general, slightly higher than the experiment data, the analysis should be useful in designing an expansion tube as an efficient energy absorber.

5. Discussions

5.1. Effect of initial elastic deformation

In the above analysis, a rigid, linear hardening material model is employed where the tube does not deform until the driving force is larger than an initial critical value F_0. In order to investigate any possible consequence of neglecting the elastic deformation, an analysis is carried out for the initial stage before F_0 is reached, with an elastic, linear hardening relationship given by:

$$\sigma = \begin{cases} E\varepsilon & \varepsilon \le \varepsilon_e \\ \sigma_s + E_P(\varepsilon - \varepsilon_e) & \varepsilon \ge \varepsilon_e \end{cases} \tag{46}$$

An axial strip OB isolated from the axisymmetrically deformed tube with the arc subtending a small angle $d\theta$ is shown in Fig. 12, with the coordinate system W-X. The circumferential membrane force and the axial bending moment can be given, respectively, as follows,

$$N_\theta = \begin{cases} \dfrac{Eh}{R_0}W & W \le W_e & (47-a) \\ N_s + \dfrac{E_p h}{R_0}\left(W - W_e\right) & W \ge W_e & (47-b) \end{cases}$$

$$M_x = \begin{cases} D\dfrac{d^2 W}{dX^2} & \kappa \le \kappa_e & (48-a) \\ M_s + D_P\left(\dfrac{d^2 W}{dX^2} - \kappa_e\right) & \kappa \ge \kappa_e & (48-b) \end{cases}$$

where $W_e = \dfrac{\sigma_s R_0}{E}, M_s = \dfrac{\sigma_s h^2}{4}$, $D = \dfrac{Eh^3}{12(1-\nu^2)}, D_P = \dfrac{E_p h^3}{12(1-\nu^2)}$ and $\kappa_e = \dfrac{M_s}{D}$. Substituting Eqs. (47-a) and (48-a) into Eq. (7), the equilibrium equation of the strip in terms of deflection is obtained for the elastic circular tube,

$$\frac{d^4 W}{dX^4} + 4k_1^4 W = 0 \tag{49}$$

where $4k_1^4 = \dfrac{Eh}{R_0^2 D}$. The general solution of Eq. (49) is given below:

$$W = e^{k_1(L-X)}\left(C_1 \cos k_1(L-X) + C_2 \sin k_1(L-X)\right)$$
$$+ e^{-k_1(L-X)}\left(C_3 \cos k_1(L-X) + C_4 \sin k_1(L-X)\right) \tag{50}$$

As the deflection and the curvature of the tube wall W at $X = 0$ are negligible, we have $C_1 = C_2 = 0$ in the general solution. Noting that the boundary conditions of the strip segment at B are $M_x = 0$, $W = W_B$, the solution is shown as

$$W = W_B e^{k_1(X-L)}\cos\left[k_1(L-X)\right] \tag{51}$$

The stroke of the die is the same as Eq. (17). The driving force can be obtained by solving the equilibrium equations of forces acting at B:

$$F = \left(\frac{\mu + \tan\gamma}{1 - \mu\tan\gamma}\right)4\pi R_0 D k_1^3 W_B \tag{52}$$
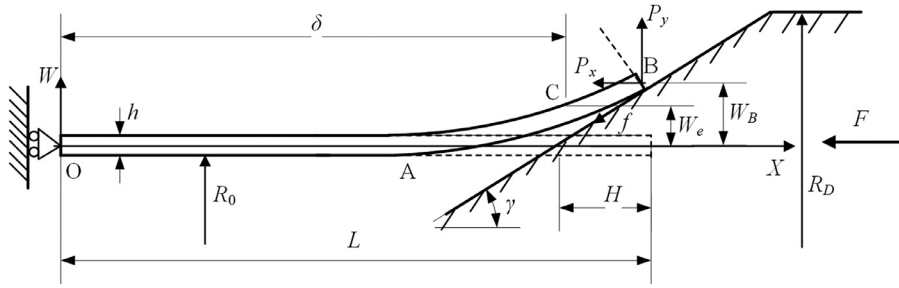
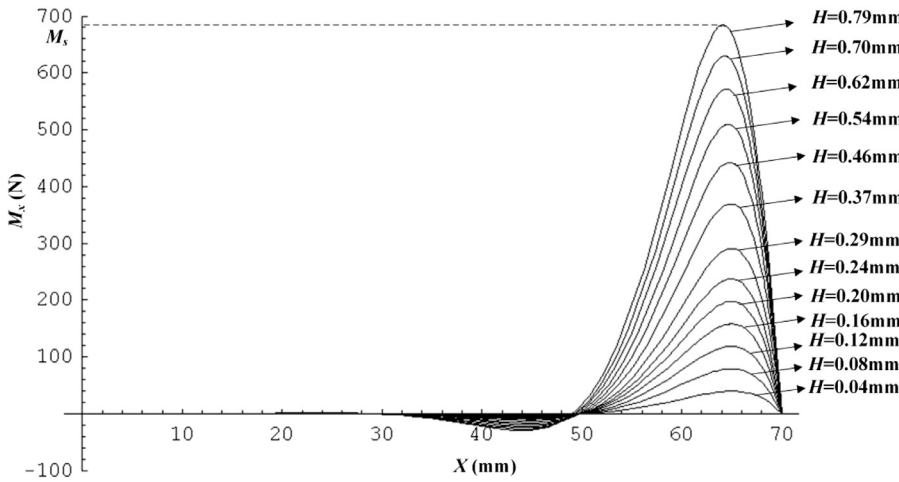**Fig. 12.** Analysis of tube deformation with elastic, linear hardening material.

Fig. 13. Evolution of the distribution of bending moment within the tube before plastic bending occurs ($0 < H < H_P$). $h = 3$ mm and $\gamma = 20°$

When the driving force increases further, it causes the initial yielding at tube tip B. The deflection of B is defined as the elastic deflection limit W_e and the corresponding stroke of the die is denoted as H_e. The strip configuration for $H > H_e$ is shown in Fig. 12. The strip can be divided into two parts: segment AC is in elastic deformation state and segment CB is in plastic. The equilibrium equation for AC is given in Eq. (49) and that for CB is obtained by substituting Eqs. (47b) and (48a) into Eq. (7). It follows that

$$\frac{\mathrm{d}^4 W_{CB}}{\mathrm{d}X^4} + 4k_2^4 W_{CB} + \frac{N_s}{R_0 D} - \frac{E_p h}{R_0^2 D} W_e = 0 \tag{53}$$

where $4k_2^4 = \frac{E_p h}{R_0^2 D}$. The *F-H* relation can be obtained by solving Eqs. (49) and (53) with suitable boundary conditions at B and the continuity conditions at C. The calculation shows that in the initial elastic deformation stage, as expected, the driving force increases linearly with the stroke, while the axial bending moment increases with the stroke and then reaches its fully plastic bending moment at stroke H_P. The evolution of bending moment distribution with the stroke increasing from 0 to H_P is illustrated in Fig. 13, where the tube thickness $h = 3$ mm and the die semi-angle $\gamma = 20°$ (abscissa X is in the axial direction of the tube).

The axial bending moment per unit length increases with the stroke and it reaches the maximum value $M_s = 675$ N at $X = 64.13$ mm, when the stroke reaches $H_P = 0.79$ mm and the driving force is $F = 13.89$ kN. The initial driving force calculated from Eq. (10) for the rigid, linear hardening model is $F_0 = 13.85$ kN and from Eq. (9) the corresponding axial bending moment reaches M_s at $X = 64.19$ mm. Comparing these values, the predictions by the rigid, linear hardening model are very close to those from the elastic, linear hardening model. This indicates that the elastic deformation may be insignificant in the large deflection of the tube during the long pushing stroke of the die and, for simplicity, a rigid, linear hardening material model can be adopted for the theoretical analysis.

Table 1

Comparison of steady-state driving force with existing experimental data and theoretical predictions. (Properties in each case can be found in Ref. [27]).

	1	2	3
R_0 (mm)	85	85	85
h (mm)	3.5	3.5	3.5
γ (°)	37.27	41.73	43.19
μ	0.25	0.1	0.05
F_s (kN) [27] (Test)	209.79	199.56	192.86
F_s (kN) [27] (Analytic)	214.41	196.64	N/A
F_s (kN) [31] (Analytic)	211.99	198.61	194.67
F_s (kN) (Present model)	212.38	196.07	189.00
Error (%)	1.2	1.7	2.0

5.2. Validation of the theoretical model

To validate the present theoretical model, the predicted steady-state driving force is compared with the existing experimental data in Ref. [27] and previous theoretical predictions by Refs. [27] and [31], as listed in Table 1. These two previous models are based on the energy method, while the current model adopts the theory of axisymmetric deformation of cylindrical shells. From Table 1, it can be found that all of the theoretically predicted steady-state driving forces agree well with the existing experimental data.

Different from the existing theoretical models, however, not only the final steady-state driving force but also the driving force as a function of the stroke of the die before the steady-state stage can be predicted by the current theoretical model. A comparison of *F-H* curves predicted by the current model and experimental curves in Ref. [1] is shown in Fig. 14 for three cases: $h = 3$ mm and $\gamma = 20°$; $h = 2$ mm and $\gamma = 10°$; and $h = 1$ mm and $\gamma = 5°$, which represent typical examples of the T-C, W-C, and W-CC modes, respectively.

For the case of $h = 3$ mm and $\gamma = 20°$, when the leading edge of the tube reaches the shoulder Q at $H_C = 4.12$ mm, the theoretical model
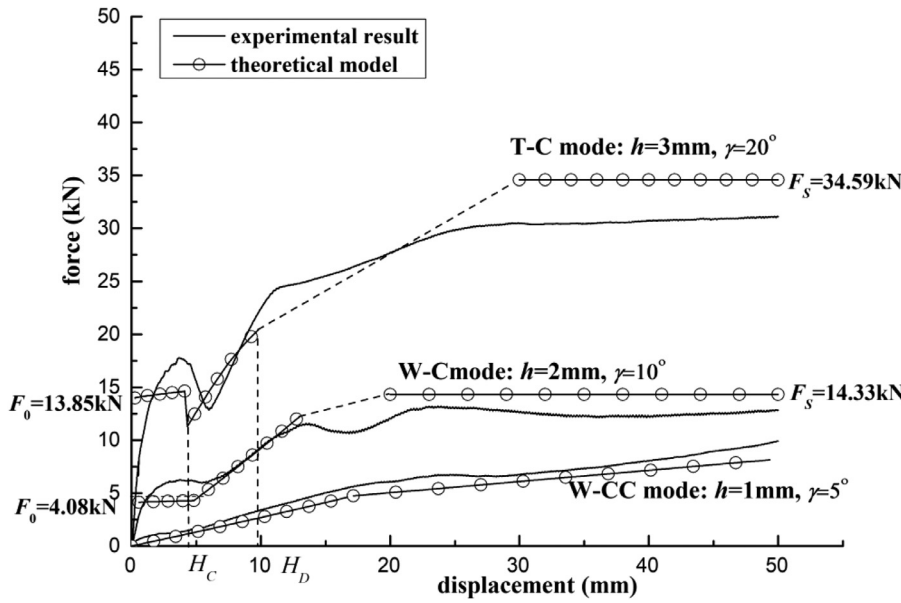
Fig. 14. Comparison of theoretically predicted and experimental *F-H* curves in Ref. [1] for the three different modes.

predicts $\phi = 14.5°$, which is lower than the die semi-angle γ. A drop of the driving force occurs at this moment owing to the sudden change in the direction of the contact force, which is a remarkable characteristic of the *F-H* curve in the T-C mode. Experimental results in Ref. [1] have confirmed this phenomenon. A steady-state force $F_s = 34.59$ kN is predicted from Eq. (45) when the steady-state deformation is reached.

For the case of $h = 2$ mm and $\gamma = 10°$, it is found that $\phi = \gamma$ when the stroke reaches $H_E = 4.82$ mm, before the leading edge of tube reaches the shoulder Q. Then the inner surface of the tube contacts the conical surface of the die, which is a distinguishing feature of the W-C mode. There is no drop in the driving force on the *F-H* curve and Eq. (45) gives a steady-state force $F_s = 14.33$ kN.

For the case of $h = 1$ mm and $\gamma = 5°$, the *F-H* curve predicted by the theoretical analysis may be approximated by two straight lines intersected at point $H_C = 17.15$ mm. The driving force always increases with the stroke; as a result, no steady-state driving force can be found in the W-CC mode, as also observed in the experiment [1].

It can be concluded that the *F-H* curves given by the theoretical analysis, which is based on a rigid, linear hardening material model, shows a reasonably good agreement with the experimental results for all the three deformation modes in the tube expansion.

5.3. Deformation modes

A series of specimens with different tube thicknesses $h = 1, 2, 3$ and 5 mm ($R_0 = 22.5$ mm) and semi-cone angles of the dies $\gamma = 5°, 10°, 15°$ and 20° ($R_D = 24$ mm) have been tested. As a result, *F-H* curves were obtained from the tests [1]. Together with the FE simulation, the three deformation modes based on the features of *F-H* curves are indicated in Fig. 15. The theoretical analysis given above also reveals that when the radius of the tubes is 22.5 mm and that of the cylindrical part of the die is 24 mm, three possible deformation modes exist, depending on geometrical parameters such as h/R_0 and γ.

In Fig. 15, the boundary between the T-C mode and the W-C mode in the $h - \gamma$ plane is obtained theoretically from the condition $\phi = \gamma$ when the tube's leading edge reaches the die shoulder Q. This theoretically obtained boundary between the T-C mode and the W-C mode is in good agreement with experiment results. For tubes of the same thickness, a larger semi-angle leads to the T-C mode and a smaller one tends to produce the W-C mode. The critical value of the die semi-angle γ between the T-C mode and the W-C mode decreases with an increase in the tube thickness. This is because the thicker tube has stronger bending rigidity, which causes a smaller angle ϕ when the tube leading edge reaches the die shoulder Q. The boundary between the W-C mode and the W-CC
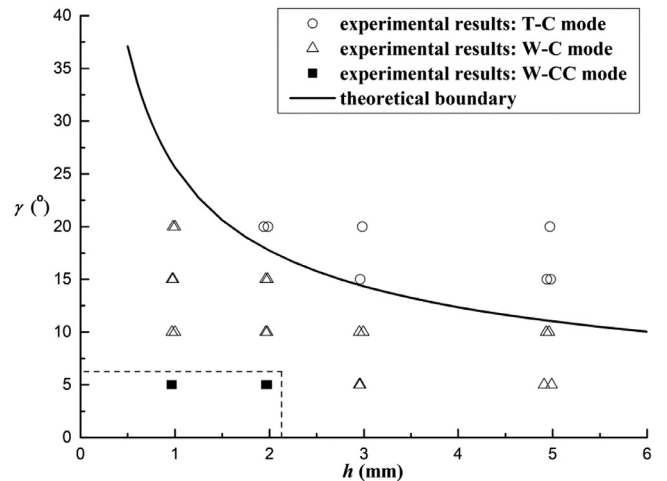

Fig. 15. Map of deformation modes in $h - \gamma$ plane, for aluminum alloy 5A06 tubes, $R_0 = 22.5$ mm and $R_D = 24$ mm.

mode is, nevertheless, less straightforward to obtain theoretically, because of the complex unloading and reversal yielding of the tube which appears in the W-C mode before its inner surface contacts the cylindrical part of the die. It was observed in the experiments that the W-CC mode existed in the cases of $\gamma = 5°$ with $h = 1$ mm and $h = 2$ mm.

5.4. Effect of strain hardening modulus and frictional coefficient on the theoretical predictions

The material used in the experiment study [1] is 5A06 aluminum, which is idealized as rigid, linear hardening with strain hardening modulus $E_p = 549$ MPa. As mentioned before, taking $E_p = 549$ MPa in the theoretical calculation is based on the equivalent principle that the areas under the stress-strain curves from the tensile test and the rigid, linear hardening model are equal for the strain in the range of 0–0.15. It means that if the material is stretched to $\varepsilon = 0.15$, the energy dissipated by the rigid, linear hardening model equals that by the actual material, as seen in Fig. 2. But actually, the material breaks at $\varepsilon = 0.198$. If we use the same equivalent principle and change the strain to the range of 0–0.198, a lower value of $E_p = 472$ MPa is obtained, as seen in Fig. 2. Besides, in the stress-strain curve, a straight line can be drawn from the
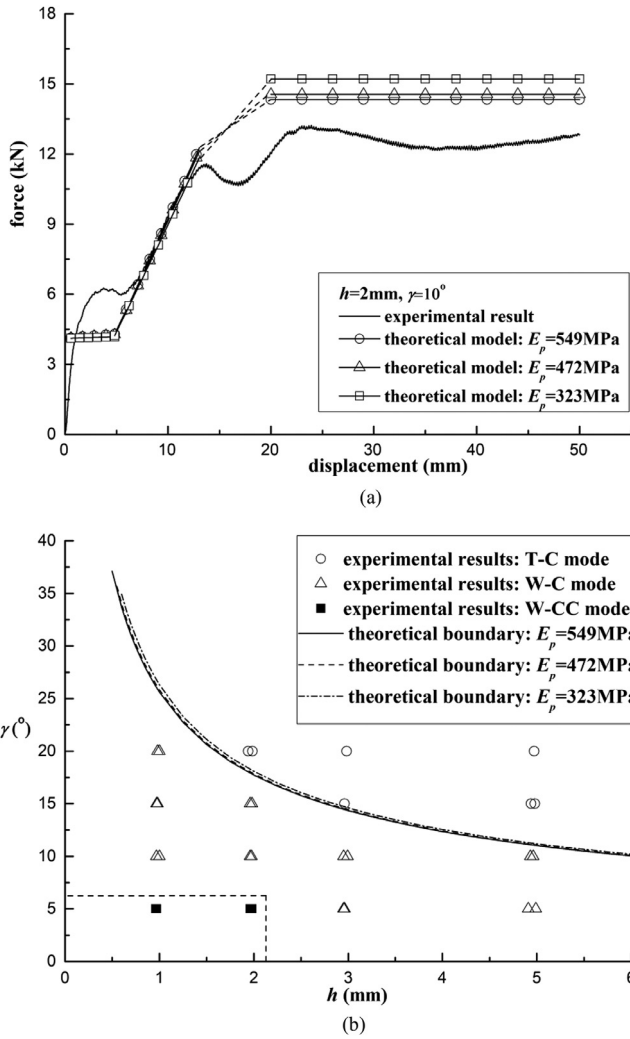
Fig. 16. Influence of different E_p on the theoretical results. (a) predicted driving force-displacement curves with different E_p. (b) predicted boundary curves between T-C mode and W-C mode with different E_p.

yield point to the breaking point and an alternative lower $E_p = 323$ MPa is obtained.

For $h = 2$ mm, $\gamma = 10°$ and $\mu = 0.05$, the predicted driving force-displacement curves with $E_p = 549$ MPa, 472 MPa and 323 MPa, respectively, are shown in Fig. 16(a) together with the experimental results. Among them the curve with $E_p = 549$ MPa is closer to the experimental result than the others, and $E_p = 549$ MPa is adopted for 5A06 aluminum in this study. Fig. 16(b) shows that when $E_p = 549$ MPa, 472 MPa and 323 MPa, respectively, the predicted boundary curves between the T-C mode and the W-C mode in the $h - \gamma$ plane are very close to each other and are in good agreement with the experiments.

It was mentioned in Section 2 that the experimental data [1] are fitted very well by choosing a coefficient of friction $\mu = 0.05$. Thus, a coefficient of friction μ=0.05 is used in the theoretical analysis. It is found that small variation in the frictional coefficient makes big changes in the results of FE simulation. For three combinations of the parameters, i.e., $h = 1$ mm and $\gamma = 5°$, $h = 2$ mm and γ=10°, and $h = 3$ mm and γ=20°, the theoretically predicted driving force versus displacement curves are shown in Fig. 17(a), (b), and (c), respectively, with $\mu = 0.0$, 0.025, 0.05, 0.075 and 0.1. It is shown that for every increment of 0.025 in the frictional coefficient, the theoretically predicted driving forces are increased considerably. For h=1 mm and γ=5°, the experiment curve is close to that with $\mu = 0.075$; for h=2 mm and γ=10°, it is close to that
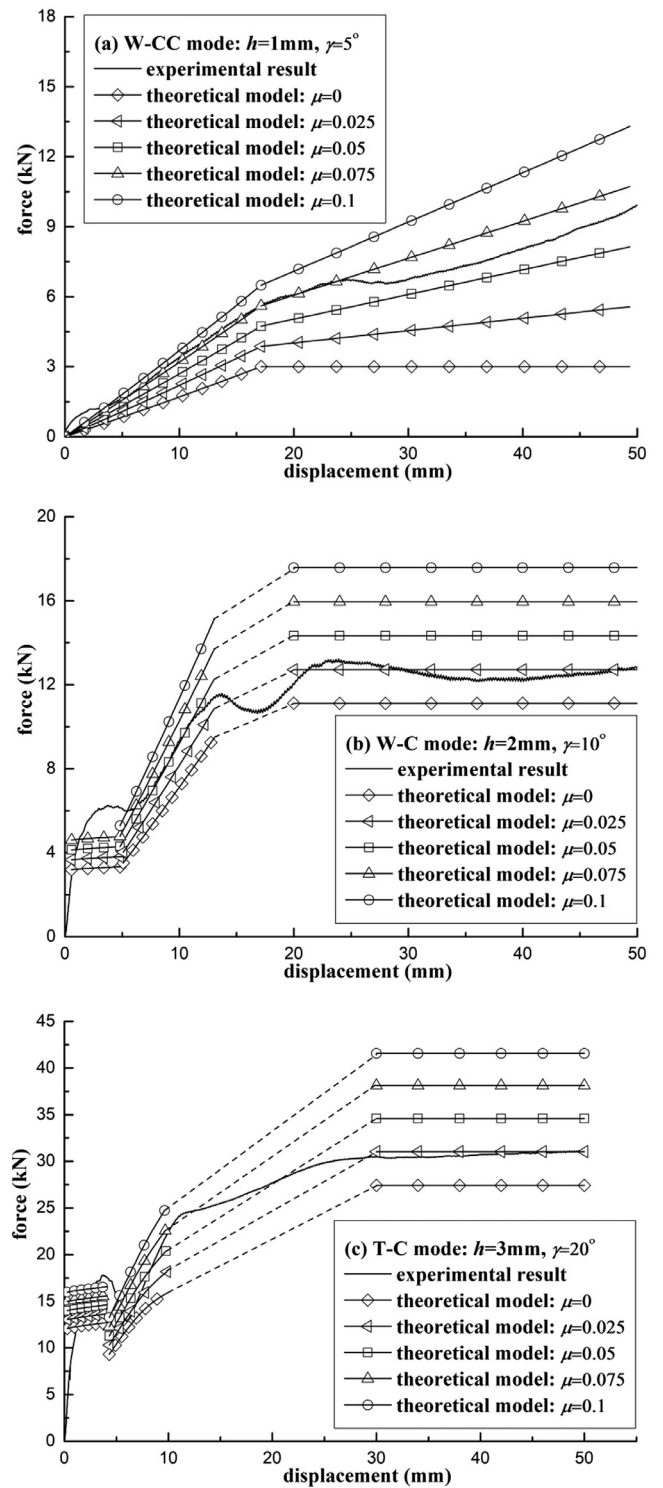

Fig. 17. Influence of the small variation in frictional coefficient on the theoretical results. (a) W-CC mode: h=1 mm and γ=5° (b) W-C mode: h=2 mm and γ=10° (c) T-C mode: h=3 mm and γ=20°

with μ=0.025; and for h=3 mm and γ=20°, it is close to μ=0.025 too. Overall, μ=0.05 is chosen in the present theoretical study.

6. Conclusions

A theoretical analysis based on the theory of axisymmetrically deformed cylindrical shell has been performed to investigate the

energy absorption characteristics of circular tubes expanded by pushing a conical-cylindrical die axially. The theoretical analysis explains the three experimentally observed deformation modes in the tube expansion process, i.e. T-C mode, W-C mode, and W-CC mode. The presence of a particular mode in tube expansion depends on the geometrical parameters, such as the value of h/R_0 (thickness/radius) and the semi-angle of dies. Accordingly, the *F-H* curves for the modes exhibit different characteristics. The boundary between the T-C mode and the W-C mode in the $h - \gamma$ plane has been determined theoretically. The deformation stages and the *F-H* curves are obtained theoretically and the steady-state driving force has been estimated. The analytical prediction agrees well with the experimental results previously reported [1]. The value of the strain hardening has been considered by choosing a modulus value so that the energy dissipated for the actual material and the idealized rigid, linear strain hardening model should be equal during the expansion process.

This theoretical study has shed new insight into the mechanics of tube deformation and will provide simple guideline in the design of such energy absorbers.

Acknowledgements

References

[1] Yang JL, Luo M, Hua YL, Lu GX. Energy absorption of expansion tubes using a conical–cylindrical die: experiments and numerical simulation. Int J Mech Sci 2010;52:716–25. https://doi.org/10.1016/j.ijmecsci.2009.11.015.

[2] Olabi AG, Morris E, Hashmi MSJ. Metallic tube type energy absorbers: a synopsis. Thin-Walled Struct 2007;45:706–26. https://doi.org/10.1016/j.tws.2007.05.003.

[3] Lu G, Yu TX. Energy absorption of structures and materials. Cambridge: Woodhead Publishing Limited; 2003.

[4] Alghamdi AAA. Collapsible impact energy absorbers: an overview. Thin-Walled Struct 2001;39:189–213. https://doi.org/10.1016/S0263-8231(00)00048-3.

[5] Alexander JM. An approximate analysis of the collapse of thin cylindrical shells under axial load. Q J Mech Appl Math 1960;13:10–15. https://doi.org/10.1093/qjmam/13.1.10.

[6] Abramowicz W, Jones N. Dynamic axial crushing of circular tubes. Int J Impact Eng 1984;2:263–81. https://doi.org/10.1016/0734-743X(84)90010-1.

[7] Wierzbicki T, Bhat SU, Abramowicz W, Brodkin D. Alexander revisited-a two folding elements model for progressive crushing of tubes. Int J Solids Struct 1992;29:3269–88. https://doi.org/10.1016/0020-7683(92)90040-Z.

[8] Pugsley A, Macaulay M. The large-scale crumpling of thin cylindrical columns. Q J Mech Appl Math 1960;13:1–9. https://doi.org/10.1093/qjmam/13.1.1.

[9] Johnson W, Soden PD, Al-Hassani STS. Inextensional collapse of thin-walled tubes under axial compression. J Strain Anal 1977;12:317–30. https://doi.org/10.1243/03093247V124317.

[10] Singace AA. Axial crushing analysis of tubes deforming in the multi-lobe mode. Int J Mech Sci 1999;41:865–90. https://doi.org/10.1016/S0020-7403(98)00052-6.

[11] Guillow SR, Lu G, Grzebieta RH. Quasi-static axial compression of thin-walled circular aluminium tubes. Int J Mech Sci 2001;43(9):2103–23. https://doi.org/10.1016/S0020-7403(01)00031-5.

[12] Karagiozova D, Jones N. Dynamic effects on buckling and energy absorption of cylindrical shells under axial impact. Thin-Walled Struct 2001;39:583–610. https://doi.org/10.1016/S0263-8231(01)00015-5.

[13] Bardi FC, Yun HD, Kyriakides S. On the axisymmetric progressive crushing of circular tubes under axial compression. Int J Solids Struct 2003;40:3137–55. https://doi.org/10.1016/S0020-7683(03)00111-2.

[14] Gupta NK, Venkatesh. Experimental and numerical studies of impact axial compression of thin-walled conical shells. Int J Impact Eng 2007;34:708–20. https://doi.org/10.1016/j.ijimpeng.2006.02.008.

[15] Zhang X, Cheng G, You Z, Zhang H. Energy absorption of axially compressed thin-walled square tubes with patterns. Thin-Walled Struct 2007;45:737–46. https://doi.org/10.1016/j.tws.2007.06.004.

[16] Nia AA, Hamedani JH. Comparative analysis of energy absorption and deformations of thin walled tubes with various section geometries. Thin-Walled Struct 2010;48:946–54. https://doi.org/10.1016/j.tws.2010.07.003.

[17] Guist LR, Marble DP. Prediction of the inversion load of a circular tube. NASA Technical Note TN-D-3622, 1966.

[18] Liu YZ, Qiu XM, Yu TX. A theoretical model of the inversion tube over a conical die. Thin-Walled Struct 2018;127:31–9. https://doi.org/10.1016/j.tws.2018.01.035.

[19] Stronge WJ, Yu TX, Johnson W. Long stroke energy dissipation in splitting tubes. Int J Mech Sci 1983;25:637–47. https://doi.org/10.1016/0020-7403(83)90073-5.

[20] Reddy TY, Reid SR. Axial splitting of circular metal tubes. Int J Mech Sci 1986;28:111–31. https://doi.org/10.1016/0020-7403(86)90018-4.

[21] Huang X, Lu G, Yu TX. On the axial splitting and curling of circular metal tubes. Int J Mech Sci 2002;44:2369–91. https://doi.org/10.1016/S0020-7403(02)00191-1.

[22] Li J, Gao G, Dong H, Xie S, Guan W. Study on the energy absorption of the expanding–splitting circular tube by experimental investigations and numerical simulations. Thin-Walled Struct 2016;103:105–14. https://doi.org/10.1016/j.tws.2016.01.031.

[23] Lu Y-H. Study of tube flaring ratio and strain rate in the tube flaring process. Finite Elem Anal Des 2004;40:305–18. https://doi.org/10.1016/S0168-874X(03)00049-0.

[24] Fischer FD, Rammerstorfer FG, Daxner T. Flaring-an analytical approach. Int J Mech Sci 2006;48(11):1246–55. https://doi.org/10.1016/j.ijmecsci.2006.06.004.

[25] Daxner T, Rammerstorfer FG, Fischer FD. Instability phenomena during the conical expansion of circular cylindrical shells. Comput Meth Appl Mech Eng 2005;194:2591–603. https://doi.org/10.1016/j.cma.2004.07.047.

[26] Almeida BPP, Alves ML, Rosa PAR, Brito AG, Martins PAF. Expansion and reduction of thin-walled tubes using a die: experimental and theoretical investigation. Int J Mach Tools Manuf 2006;46:1643–52. https://doi.org/10.1016/j.ijmachtools.2005.08.018.

[27] Shakeri M, Salehghaffari S, Mirzaeifar R. Expansion of circular tubes by rigid tubes as impact energy absorbers: experimental and theoretical investigation. Int J Crashworthiness 2007;12:493–501. https://doi.org/10.1080/13588260701483540.

[28] Seibi AC, Barsoum I, Molki A. Experimental and numerical study of expanded aluminum and steel tubes. Procedia Eng 2011;10:3049–55.

[29] Al-Abri OS, Pervez T. Structural behavior of solid expandable tubular undergoes radial expansion process-analytical, numerical, and experimental approaches. Int J Solids Struct 2013;50:2980–94. https://doi.org/10.1016/j.ijsolstr.2013.05.013.

[30] Yan J, Yao S, Xu P, Peng Y, Shao H, Zhao S. Theoretical prediction and numerical studies of expanding circular tubes as energy absorbers. Int J Mech Sci 2016;105:206–14. https://doi.org/10.1016/j.ijmecsci.2015.11.022.

[31] Liu Y, Qiu XM. A theoretical study of the expansion metal tubes. Int J Mech Sci 2016;114:157–65. https://doi.org/10.1016/j.ijmecsci.2016.05.014.

[32] Li J, Gao GJ, Dong H, Xie S, Guan W. Study on the energy absorption of the expanding-splitting circular tube by experimental investigations and numerical simulations. Thin-Walled Struct 2016;103:105–14. https://doi.org/10.1016/j.tws.2016.01.031.

[33] Chahardoli S, Nia AA. Investigation of mechanical behavior of energy absorbers in expansion and folding modes under axial quasi-static loading in both experimental and numerical methods. Thin-Walled Struct 2017;120:319–32. https://doi.org/10.1016/j.tws.2017.09.013.

[34] Liu YZ, Qiu XM, Wang W, Yu TX. An improved two-arcs deformational theoretical model of the expansion tubes. Int J Mech Sci 2017;133:240–50. https://doi.org/10.1016/j.ijmecsci.2017.08.036.

[35] Hodge PG. Plastic analysis of structures. McGraw-Hill; 1959.